Published in final edited form as:
J Med Chem. 2008 October 23; 51(20): 6348–6358. doi:10.1021/jm800435s.

Towards optimization of the linker substructure common to transthyretin amyloidogenesis inhibitors using biochemical and structural studies

Steven M. Johnson[1], **Stephen Connelly**[2], **Ian A. Wilson**[2,3], and **Jeffery W. Kelly**[1,3,*]

1*Department of Chemistry, The Scripps Research Institute, BCC 265, 10550 N. Torrey Pines Rd., La Jolla, CA 92037*

2*Department Molecular of Biology, The Scripps Research Institute, BCC 265, 10550 N. Torrey Pines Rd., La Jolla, CA 92037*

3*The Skaggs Institute for Chemical Biology, The Scripps Research Institute, BCC 265, 10550 N. Torrey Pines Rd., La Jolla, CA 92037*

Abstract

To develop potent and highly selective transthyretin (TTR) amyloidogenesis inhibitors, it is useful to systematically optimize the three substructural elements that compose a typical TTR kinetic stabilizer: the two aryl rings and the linker joining them. Herein, we evaluated 40 bisaryl molecules based on 10 unique linker substructures to determine how these linkages influence inhibitor potency and selectivity. These linkers connect one unsubstituted aromatic ring to either a 3,5-$\mathbf{X}_2$ or a 3,5-$\mathbf{X}_2$-4-OH phenyl substructure (**X**=Br or CH_3). Co-consideration of amyloid inhibition and *ex vivo* plasma TTR binding selectivity data reveal that direct connection of the two aryls, or linkage through non-polar *E*-olefin or $–CH_2CH_2–$ substructures generates the most potent and selective TTR amyloidogenesis inhibitors exhibiting minimal undesirable binding to the thyroid hormone nuclear receptor or the COX-1 enzyme. Five high-resolution TTR•inhibitor crystal structures (1.4−1.8 Å) provide insight into why such linkers afford inhibitors with greater potency and selectivity.

Introduction

An aging-associated decline in protein homeostasis capacity can lead to loss-of-function diseases associated with excessive misfolding and biological degradation or degenerative diseases linked to protein aggregation, especially when proteome maintenance is further challenged by mutation(s) or aberrant protein modifications.[1-4] Transthyretin (TTR) is one of more than thirty human amyloidogenic proteins whose rate-limiting dissociation, misfolding and misassembly into a variety of aggregate structures, including cross-β-sheet amyloid fibrils, appears to cause a variety of degenerative gain-of-toxic-function maladies.[5-7] The mechanism

* To whom correspondence should be addressed: Tel: 858−784−9605. Fax: 858−784−9610. E-mail: jkelly@scripps.edu.

Supporting Information Available:
Efficacy scoring of the previously evaluated aryl-**X** substructure optimization library, detailed synthetic schemes, procedures, and characterization data for all compounds, calculated phenolic pKa values, and tabulation of compound purity as determined by C_4 and C_{18} RP-HPLC. This material is available free of charge via the Internet at http://pubs.acs.org.

Protein Data Bank Accession Codes.
Atomic coordinates have been deposited in the RCSB Protein Data Bank (www.pdb.org) and are available under accession codes 3CN0 (WT-TTR in complex with **2c**), 3CN1 (WT-TTR in complex with **2d**), 3CN2 (WT-TTR in complex with **3d**), 3CN3 (WT-TTR in complex with **5d**), 3CN4 (WT-TTR in complex with **10d**),.

of proteotoxicity and whether toxicity results from TTR aggregation inside and/or outside the cell are key questions that remain unanswered.

Wild type transthyretin (WT-TTR) aggregation-associated proteotoxicity appears to cause senile systemic amyloidosis, a cardiomyopathy that affects up to 10−20% of the population over age 65.[7-10] Mutant TTR deposition leads to familial amyloid cardiomyopathy (FAC) in 3−4% of African Americans carrying at least one V122I-TTR allele.[11, 12] Familial amyloid polyneuropathy (FAP) affects thousands of V30M-TTR carriers, as well as more individuals harboring one of nearly one hundred rarer TTR mutations.[13] The rare central nervous system selective amyloidoses (CNSA) appear to be caused by D18G- and A25T-TTR mutations.[14-16] Without treatment, the TTR amyloidoses are fatal.

The only treatment currently available for FAP is gene therapy mediated by liver transplantation,[17-19] in which the heterozygotic FAP mutant TTR/WT-TTR liver secreting TTR into the blood is replaced by a WT-TTR/WT-TTR secreting liver. This procedure dramatically decreases mutant plasma TTR levels and halts disease progression in most patients, at least initially. A drawback of this strategy is that WT-TTR deposition often continues post-transplantation in the heart, leading to cardiomyopathy, likely reflecting an age-dependent decline in protein homeostasis capacity.[1, 20] Because of the limited applicability of liver transplantation (must be completed early in the course of disease) and the requirement for life-long immune system suppression, an alternative, generally applicable, oral small molecule therapy for all the TTR-based amyloid diseases is highly desirable.[7]

Transthyretin transports the vitamin A-retinol binding protein (RBP) complex and thyroxine (T_4) in blood. The tetrameric quaternary structure of transthyretin is composed of 127-amino acid, β-sheet rich subunits that exhibit two different dimer-dimer interfaces (Figure 1).[7, 21-26] The energetically weaker dimer interface in WT-TTR creates two funnel-shaped pockets where thyroxine binds. However, because of the high concentration of TTR and the presence of two other thyroxine carrier proteins (thyroxine binding globulin and albumin), <1% of these sites in the TTR tetramers are actually occupied by T_4.

Numerous small molecules, typically composed of two differentially-substituted aromatic rings connected by linkers of variable chemical composition (Figure 2), are known to avidly bind to the unoccupied T_4 sites within TTR (displaying either positive-, non-, or negative-cooperativity).[7, 27-38] Such ligands typically bear polar substituents on their aryl rings that enable electrostatic interactions with the Lys-15 ε-NH_3^+ and/or the Glu-54 carboxyl group(s) positioned at the periphery of the outer cavity of the TTR T_4 binding site. These polar substituents can also hydrogen bond to the Ser-117 or Thr-119 hydroxyl groups in the inner binding cavity when an aryl ring bearing polar substituents is placed into the inner cavity. Each T_4 binding site is composed of three pairs of symmetric hydrophobic depressions, referred to as the halogen binding pockets (HBPs), wherein the iodine atoms of T_4 reside (Figure 1).[26] One pair is located in each of the smaller inner and larger outer binding site cavities, while the third (HBP-2/2') is found at the interface between the two cavities. In the highest affinity inhibitors, one or both rings display halogen or alkyl substituents that bind to the hydrophobic HBPs.

In binding to either one or both of the T_4 sites, small molecules non-covalently bridge neighboring monomeric subunits *via* specific hydrophobic and electrostatic interactions, stabilizing the weaker dimer-dimer interface (Figure 1).[7, 21-26] Binding to one site imposes kinetic stability on the entire native quaternary structure of TTR by differentially stabilizing its tetrameric state over its dissociative transition state, precluding rate-limiting tetramer dissociation and amyloidogenesis from commencing under physiological conditions.[7, 23, 24, 39, 40] There is good reason to be optimistic that such small molecule kinetic stabilizers

will be efficacious against TTR amyloid disease, since a similar interallelic *trans*-suppression kinetic stabilization strategy is known to ameliorate familial amyloid polyneuropathy. In interallelic *trans*-suppression, compound heterozygotes, where one allele codes for the disease-associated V30M-TTR variant (associated with high FAP penetrance) and another for T119M-TTR, are protected from FAP as a consequence of inclusion of T119M subunits into the heterotetramers. Inclusion of T119M subunits into tetramers otherwise composed of amyloidogenic subunits kinetically stabilizes the tetrameric structure of TTR, preventing tetramer dissociation required for amyloidogenesis and the onset of FAP symptoms.[7, 39, 41-43]

We have designed and synthesized three small molecule libraries to optimize the three substructures comprising a typical TTR amyloidogenesis inhibitor (Figure 2): the two aromatic rings and the linker connecting them. In each case, at least one fixed substructure in the library was purposefully non-optimal to generate a wider range of amyloidogenesis inhibitor activities and TTR plasma binding selectivities that are collectively utilized to rank order the individual substructures. The intention of this effort is to generate information about optimal components for kinetic stabilizers which can ultimately be used to generate clinical candidates. This data should allow us to be able to predict the structures of potent and selective TTR amyloidogenesis inhibitors that are largely devoid of thyroid hormone receptor and cyclooxygenase-1 (COX-1) activity, which are undesirable characteristics for cardiomyopathy applications. Investing the effort in this three part series to find the best substructure building blocks should increase the probability of identifying TTR kinetic stabilizers with desirable pharmacological properties going forward.

In the recently published first paper in this series, we established the desirability of the 3,5-$\mathbf{X}_2$-phenyl, the 3-**X**-4-OH-phenyl, and the 3,5-$\mathbf{X}_2$-4-OH-phenyl as optimal aryl-**X** substructures (Figure 2; where **X**=CH_3, F, Cl, Br, I) based on both amyloidogenesis inhibition and TTR plasma binding selectivity data.[27] Moreover, these otherwise unsubstituted benzoxazoles bearing these aryl-**X** substructures at the 2-position are largely devoid of undesirable thyroid hormone receptor or COX-1 binding.

Herein, we focus on rank ordering TTR kinetic stabilizer linker-**Y** substructures (Figure 2) using biochemical and, to a lesser extent, structural data. For this purpose, we utilize four potent aryl-**X** substructures, recognized as optimal by the first paper in this series, and a non-optimal unsubstituted aryl-**Z** substructure in all library components to provide a range of efficacies. In total, 36 molecules were constructed (Figure 3, *bottom*) based on eight acyclic linker-**Y** substructures as well as a direct aryl-**X**–aryl-**Z** connection (i.e. biphenyl), and these were compared to the 2-arylbenzoxazoles (**1a**-**d**) to evaluate a second direct aryl-aryl linkage and to provide continuity with study 1, where these compounds were utilized. Each candidate was synthesized according to previously published procedures (detailed synthetic schemes, procedures, and characterization data are reported in the Supporting Information). Consideration of both amyloid inhibition data and *ex vivo* plasma TTR binding selectivity data reveal that direct connection of the two aryls, or linkage through non-polar *E*-olefin or –CH_2CH_2– substructures generates the most potent and selective TTR amyloidogenesis inhibitors – series that largely lack undesirable binding to the thyroid hormone nuclear receptor and the COX-1 enzyme. Five high-resolution TTR•inhibitor crystal structures (1.4−1.8 Å) were determined that, along with molecular mechanics simulations, provide insight into why such linkers impart TTR amyloidogenesis inhibitors with greater potency and binding selectivity.

Results

Small molecule-mediated inhibition of WT-TTR amyloidogenesis

The compounds composing the linker-**Y** optimization library (Figure 4) were first evaluated for their ability to inhibit WT-TTR amyloidogenesis using the acid-mediated aggregation assay, performed according to the procedures reported in the preceding aryl-**X** substructure optimization study.[27] Briefly, a physiologically relevant concentration of WT-TTR (3.6 μM) was pre-incubated with a candidate inhibitor (7.2 μM) and then subjected to partial acid denaturation under conditions that enable approximately 90% of WT-TTR to aggregate in the absence of inhibitor after 72 h (pH 4.4, 37 °C). Acidic conditions were used to enable amyloidogenesis on a convenient laboratory timescale – the process is much slower at pH 7.5. The extent of TTR aggregation (Figure 4) was monitored by measuring sample turbidity in the presence of the test compound, expressed as a percentage of protein aggregation observed in inhibitor free samples (assigned as 100% fibril formation). Of the 36 new compounds evaluated, 16 exhibit potent inhibition of WT-TTR aggregation (<20% TTR aggregation: i.e. >80% inhibition). Since the goal of this effort was not to identify clinical candidates, the efficacies of the compounds were not evaluated at pH 7.5.

Binding selectivity of amyloidogenesis inhibitors to TTR in human blood plasma

Sixteen of the potent TTR aggregation inhibitors (Figure 4; not counting the previously evaluated 2-arylbenzoxazoles **1a-d**) as well as the most potent linker 10 containing inhibitor were further evaluated for their ability to bind selectively to TTR in the blood using an *ex vivo* TTR plasma binding selectivity assay, reported previously[27] Briefly, the candidate inhibitor (10.8 μM) is incubated in human blood plasma in the dark at 37°C for 24 h. Transthyretin, with any bound inhibitor, is then captured by a resin-conjugated anti-TTR antibody and any unbound material is washed away (including weakly or nonspecifically bound inhibitors). The captured TTR•$(\text{inhibitor})_n$ complex is then dissociated from the antibody under alkaline conditions and the TTR and inhibitor stoichiometry is quantified by RP-HPLC. Results represent the average stoichiometry of inhibitor bound to TTR in blood plasma (Figure 4, lower italicized values), the maximum value being 2, owing to the presence of the two thyroxine binding sites in each tetramer. Seven of these potent inhibitors (not including **1a-d**) display average binding stoichiometries that exceed 1 equivalent bound per TTR tetramer, three of which are exceptionally selective and display >1.5 equivalents bound (**3d**, **4d**, and **5d**). An additional four compounds display average binding stoichiometries between 0.5 and 1.0 (**3c**, **4c**, **7d**, and **9d**), values that are likely acceptable for a clinical candidate, while the remainder exhibit minimal TTR binding selectivity (<0.5 equivalents bound per tetramer). Human plasma TTR binding selectivity data is better than in vitro IC_{50} inhibition data for finer SAR distinctions because potent inhibitors can, and sometimes do, bind to plasma proteins other than TTR rendering them useless as TTR kinetic stabilizers.

Evaluating the potent TTR amyloidogenesis inhibitors for COX-1 enzymatic inhibition and binding to the thyroid hormone nuclear receptor

The 16 potent TTR aggregation inhibitors (Figure 4; excluding the previously evaluated 2-arylbenzoxazoles **1a-d**) as well as the most potent linker 10 containing inhibitor were further evaluated for their ability to inhibit COX-1 enzymatic activity and also to competitively bind to the thyroid hormone nuclear receptor. These analyses were contracted out to the Cerep laboratories in Redmond, WA, USA (refer to the Experimental section for a detailed description of the assay protocols).[27, 44, 45] For the COX-1 inhibition analyses, results represent the % inhibition of arachidonic acid conversion to PGE_2 due to competitive binding of test compound to COX-1 (Figure 5, lower, black values). Of the 17 compounds evaluated, all but four display <5% inhibition of COX-1 activity; compounds **2c**, **3c**, **4c**, and **6c** display slight to substantial (23−66%) COX-1 inhibition. For the thyroid hormone receptor binding analyses, the %

displacement of [^{125}I]-labeled triiodothyronine (T_3, the primary thyroid hormone) was determined from competitive binding of test compound to the thyroid hormone receptor (Figure 5, red, italicized values). Of the 17 compounds evaluated, nearly all display minimal (<10%) inhibition of T_3 binding to the thyroid hormone nuclear receptor; only compound **2d** significantly displaces T_3 (28%). While these criteria were not used to rank order the linker-**Y** substructures, the lack of these substructure activities is highly desirable for cardiomyopathy applications.

X-ray crystallographic analysis of WT-TTR bound to inhibitors 2c, 2d, 3d, 6d, and 10d

Crystal structures of compounds **2c**, **2d**, **3d**, **6d**, and **10d** in complex with WT-TTR were determined to 1.4−1.8 Å resolution (Table 1). The observed electron densities in all five structures allowed unambiguous placement of the 3,5-$\mathbf{X_2}$-4-OH aryl rings, which bound rigidly in either the inner or outer TTR binding cavities. Inhibitor **2c** binds in what is referred to as the 'forward' binding mode, with its 3,5-dimethyl-4-hydroxyphenyl substructure occupying the inner cavity of the thyroxine binding site (Figure 6). In such an orientation, the methyl substituents of **2c** extend into the two halogen binding pockets located in the inner binding cavity (HBP-3 and 3'), while the 4-OH creates a hydrogen bonding network that bridges the Ser-117 and 117' side-chain hydroxyls of adjacent TTR subunits and involves an ordered water molecule. In contrast, inhibitors **2d**, **3d**, **6d**, and **10d** bind in the 'reverse' binding mode, wherein their bromines extend into the outer cavity HBPs 1 and 1' (Figure 6), allowing their phenolate substituents to interact with the Lys-15 and 15' ε-NH_3^+ groups. In the **6d** co-crystal structure, a unique ordered water molecule is located between the Ser-117 and 117' hydroxyls (2.49 Å from each). While additional ordered water molecules have been modeled elsewhere, they do not make significant interactions with any of the bound inhibitors. Whether the ligands are bound in the forward or reverse orientations, the linkage substructures are positioned in the hydrophobic environment of HBP-2 and 2'. In all five structures, the aryl-**X** and aryl-**Z** rings are non-planar with respect to each other, adopting out-of-plane orientations of 35° for **2c** and **2d**, 40−42° for **3d**, 59° for **6d**, and 42−45° for **10d** (structures of the previously evaluated inhibitors **1a**, **1c**, and **1d** display ring-ring torsional angles of 17−22°).[27]

Discussion

Optimal linker substructures for creating potent TTR amyloidogenesis inhibitors exhibiting high TTR binding selectivity in blood

Because the structure-activity relationship (SAR) data generated by this linker-**Y** optimization study will ultimately be used in concert with analogous SAR data from the aryl-**X** and aryl-**Z** optimization studies to predict the structures of highly potent and selective TTR amyloidogenesis inhibitors, we considered the collective activities of the four compounds in each linker series in order to rank order linker efficacy (Figure 4). In this substructure ranking calculation that collectively considers inhibition efficacy and plasma TTR binding selectivity, we first averaged the % fibril formation (% $F.F._{ave}$) and plasma TTR binding stoichiometry ($P.S._{ave}$) values of the four compounds within a linker series. Compounds that were not tested in the plasma selectivity assay because they permit >20% aggregation of TTR were assigned plasma stoichiometry values of 0 for averaging purposes, as experience demonstrates that poor aggregation inhibitors typically display little, if any, binding to TTR in blood plasma. To obtain an efficacy score for each linker substructure, the % $F.F._{ave}$ and $P.S._{ave}$ values were then input into equation **1**.

$$\text{Efficacy Score}=\frac{(100\% - \%F.F._{ave}) \times (1+P.S._{ave})}{300\%} \quad \text{Eq. 1}$$

Subtraction of the % $F.F._{ave}$ values from 100% is done to convert the data into % inhibition. The $P.S._{ave}$ values are adjusted by adding 1 in order to be able to differentiate inhibitors with

plasma binding stoichiometries of 0 from each other based on % inhibition data. Division by 300% restricts the efficacy scores to a range between 0 and 1, the latter being the best score. Consideration of both inhibitor efficacy and plasma binding selectivity in this fashion affords a clear rank-ordering of the linker substructures, with series **1** (2-arylbenzoxazoles) being the most potent and selective, decreasing to the least efficacious represented by series **10** (bisarylamide). We also retrospectively applied this scoring system to data previously recorded[27] in studies focused on rank ordering the aryl-**X** substructures and found it ranks those substructures strictly analogously to the rankings derived from a qualitative assessment (data presented in Figure S1 in the Supporting Information).

The potent and selective TTR amyloidogenesis inhibitors in the linker optimization library minimally interact with COX-1 enzyme and thyroid hormone receptor

Since many of the potent TTR amyloidogenesis inhibitors in the linker-**Y** optimization library bear resemblance to some common non-steroidal anti-inflammatory drugs (NSAIDs), their ability to inhibit COX-1 activity was evaluated. COX-1 binding is undesirable, especially for familial amyloid cardiomyopathy patients, as NSAID activity can further compromised renal blood flow.[37, 46, 47] Of the 17 compounds evaluated (not including **1a-d** previously evaluated), only 4 display appreciable inhibition of COX-1 activity (Figure 5, lower, black percentages) and since all 4 are comprised of different linkers, it is safe to conclude that the linker correlation with COX-1 activity is poor. The 3,5-$(CH_3)_2$-4-hydroxyphenyl substructure common to those compounds exhibiting NSAID activity suggests that future amyloidogenesis inhibitors bearing this aryl-**X** substructure should be pursued with caution.

Since many of the potent TTR amyloidogenesis inhibitors in the linker optimization library are comprised of thyroid hormone-like aryl-**X** rings, we screened for this activity. The only potent compound displaying binding to the thyroid hormone receptor is **2d**, which displaces 28% of bound T_3 (Figure 5, upper, red values).[45] Based on these data, it is not clear that any of the linkers confer a risk for targeting the thyroid hormone nuclear receptor.

Structural characterization of potent and selective TTR amyloidogenesis inhibitors comprising a variety of linkers

Examination of numerous TTR•$(ligand)_2$ co-crystal structures deposited in the Protein Data Bank reveals the general trend that the two aryl rings of the ligands are typically oriented out-of-plane from one another.[26-29, 34, 36, 38, 40, 48] Not surprisingly, this trend persists in the five crystal structures generated by this study (Figure 6), as well as in the three previously reported 2-arylbenzoxazole (compounds **1a**, **1c**, and **1d**) crystal structures.[27] The aryl-**X** and aryl-**Z** rings adopt out-of-plane orientations with respect to each other, ranging from 17−22° for the 2-arylbenzoxazoles (**1a**, **1c**, and **1d**) to 59° for biphenyl ether **6d**. It is likely that any kinetic stabilizer binding to TTR will need to adopt similar out-of-plane aryl conformations to achieve optimal protein-ligand interactions.

Optimal TTR-ligand interactions could also be affected by the differences in structure and energy between the preferred conformations of the free versus bound ligands. Simple molecular mechanics simulations suggest that the preferred conformations of unbound **3d** and **6d** are similar in structure and energy to their bound conformations and, not surprisingly, both are relatively potent TTR aggregation inhibitors. However, in cases where the bound conformation of a ligand is markedly different from its free conformation, the higher energy of the bound ligand could significantly affect binding affinity. This could help partially explain why the series **7**−**10** compounds are generally poor inhibitors of TTR aggregation. Examination of these scaffolds reveals that the rotational energy barriers for aryls adjacent to a linking NH group are significantly higher than when adjacent to carbon or oxygen atoms, with a preferred orientation of the aryl being co-planar with the N-H bond. Using compound **10d** (a poor

inhibitor) as an example, the conformational energy penalty to achieve the desired aryl-aryl orientation is ~1.2 kcal/mol higher than that required for binding of **2d** (a good inhibitor). It is likely that other factors substantially influence ligand binding affinity and inhibitor potency as well, notably desolvation energies, which are difficult to predict.

Irrespective of whether a compound binds in the forward or reverse orientation, its linker substructure will be positioned within the primarily hydrophobic environment of HBP-2 and 2'. This may partially explain why compounds composed of polar linkers (in particular, series **7**−**10**) are generally less potent than their non-polar linkage counterparts (series **1**−**4**); since occupancy of the hydrophobic HBP-2 and 2' region of the thyroxine binding site by the hydrophilic linkers is likely unfavorable due to linker desolvation energies that are not compensated for. Thus, it appears that the hydrophobicity, and to a lesser extent the conformational propensities of the linkers, justifies their structure-activity relationships or rankings.

In the recently published aryl-**X** substructure optimization study, we hypothesized, based on structural data, that high pKa phenols like 3,5-$(CH_3)_2$-4-hydroxyphenyl would occupy the inner binding cavity of the thyroxine binding site (H-bonding with Ser-117 and 117' hydroxyl groups), whereas low pKa phenols, such as 3,5-Br_2-4-hydroxyphenyl, would bind to the outer cavity because their phenolates could interact with the Lys-15 and 15' side chain ε-NH_3^+ groups in the absence of dominating substituents on the aryl-**Z** ring.[27] This hypothesis is rigorously supported by the five co-crystal structures obtained in this study, moreover the diversity of linkers in these structures suggests that the linker has little influence on directing inhibitor binding orientation.

In the **2c** co-crystal structure (Figure 6), the 3,5-$(CH_3)_2$-4-hydroxyphenyl aryl (Figure S2, phenol pKa calculated to be 9.85) resides in the inner cavity and hydrogen bonds with the Ser-117 and 117' hydroxyls. In the four other co-crystal structures, the 3,5-Br_2-4-hydroxyphenyl substructures of **2d**, **3d**, **6d**, and **10d** (Figure S2, pKa's of their phenols calculated to be 5.98, 6.39, 6.33, and 6.50, respectively) are found in the outer binding cavity–their putative phenolates interacting with the Lys-15 and 15' side chain ε-NH_3^+ groups (Figure 6). Since they are calculated to have comparable pKa values, we expect that fluoro, chloro, and iodo analogues would also bind in similar reverse orientations in the absence of dominating substituents on the aryl-**Z** ring.

Concluding Remarks

A linker-**Y** substructure optimization library featuring 10 different linkers comprising 40 small molecules, each composed of two aromatic rings (one of which was always unsubstituted) revealed that direct linkage of two aryl rings (i.e. biphenyls and 2-arylbenzoxazoles), or linkage through a non-polar substructure such as an *E*-olefin or a – CH_2CH_2– bridge, produced the most potent and selective transthyretin amyloidogenesis inhibitors. Several of these display near maximal TTR plasma binding stoichiometries (>1.5 equivalents bound per tetramer), which is even more impressive when one considers that adding substituents to the unsubstituted aryl-**Z** ring will likely further enhance binding affinity, potency, and selectivity. These kinetic stabilizers proved to be largely devoid of thyroid hormone receptor binding and COX-1 activity, revealing that these linker substructures could be incorporated into clinical candidates for TTR cardiomyopathy applications. Structural data rationalize why hydrophobic linkers are ranked highest, to maximize the hydrophobic effect contribution to binding energy due to their placement in the vicinity of the hydrophobic HBPs 2 and 2'. The crystallographic results rigorously support the hypothesis that the orientational binding preferences of inhibitors are strongly influenced by the ionization states of the 4-hydroxy substituent. In combination with the data from the first[27] and third substructure optimization studies (aryl-**X** and aryl-**Z**

substructures, respectively), the linker substructure optimization data reported herein should allow us to predict the structures of potent and selective TTR amyloidogenesis inhibitors that lack undesirable thyroid hormone receptor and COX-1 activity. When we do produce clinical candidates, it will be highly desirable to collect cellular and organismal toxicity data on them.

Experimental

General synthetic methods

Detailed synthetic schemes, procedures, and characterization data are presented in the Supporting Information. Unless otherwise stated, all chemicals were purchased from commercial suppliers and used without further purification. Reaction progress was monitored by thin-layer chromatography on silica gel 60, F254 coated glass plates (EM Sciences). Flash chromatography was performed using 230−400 mesh silica gel 60 (EM Sciences). NMR spectra were recorded on a Bruker 500 MHz spectrometer. Chemical shifts are reported in parts per million downfield from the internal standard Me_4Si (0.0 ppm) for $CDCl_3$ solutions, whereas d_6-DMSO and CD_3OD solutions are calibrated to the solvent peaks at 2.49 and 3.31 ppm for the ^{1}H-NMR spectra, respectively, and 39.52 and 49.00 ppm for the ^{13}C-NMR spectra, respectively. Reverse phase high performance liquid chromatography (RP-HPLC) was performed using a Waters 600 E multi-solvent delivery system employing a Waters 486 tunable absorbance detector and 717 autosampler. Samples were chromatographically separated using a ThermoHypersil-Keystone Betabasic-18 column (model 71503−034630, 150 Å pore size, 3 μm particle size), eluting with a H_2O:CH_3CN gradient solvent system. Linear gradients were run from either 100:0, 80:20, or 60:40 A:B to 0:100 A:B (A = 95:5 H_2O:CH_3CN, 0.25% trifluoroacetic acid (TFA); B = 5:95 H_2O:CH_3CN, 0.25% TFA). Final compound purities were additionally evaluated under distinct RP-HPLC conditions by chromatographically separating samples using a Vydac-C_4 column (model 214TP5415, 300 Å pore size, 5 μm particle size), eluting with a H_2O:MeOH gradient solvent system. Linear gradients were run from 100:0 to 0:100 C:D (C = 99.75% H_2O, 0.25% TFA; D = 100% MeOH). For preparatory HPLC purification, samples were chromatographically separated using a Vydac C_{18} column (model 218TP1022, 300 Å pore size, 5 μm particle size) employing the above H_2O:CH_3CN solvent systems (without TFA). All mass spectrometry data were collected at the Scripps Research Institute Center for Mass Spectrometry.

Evaluating small molecule-mediated inhibition of WT-TTR amyloidogenesis

WT-TTR was purified from an *E. coli* expression system as described previously.[49] To a 495 μL aliquot of 0.4 mg/mL WT-TTR (7.2 μM, 10 mM phosphate, pH 7.0, 100 mM KCl, 1 mM EDTA) in a disposable cuvette was added 5.00 μL of a 1.44 mM DMSO solution of test compound and the sample was vortexed briefly. After incubating for 30 min at ambient temperature, the pH of the sample was lowered to 4.4 by addition of 500 μL of acidic buffer (100 mM acetate, pH 4.2, 100 mM KCl, 1 mM EDTA) and the solution was briefly vortexed and incubated in the dark for 72 h at 37°C (final protein and inhibitor concentrations were 3.6 and 7.2 μM, respectively). The sample was then vortexed to evenly distribute any precipitate, and the turbidity was measured at 400 nm on a Hewlett Packard model 8453 UV-Vis Spectrophotometer. The extent of WT-TTR aggregation (% fibril formation, *f.f.*; % inhibition = 100 - %*f.f.*) was determined by comparing the sample turbidity in the presence of small molecule as a percentage of control WT-TTR sample incubated with 5.00 μL of pure DMSO (representing 100% aggregation, 0% inhibition). All samples were assayed in at least quintuplicate, with average values obtained presented in Figure 3 (errors are typically less than ±5 percentage points).

Evaluating the binding selectivity of amyloidogenesis inhibitors to TTR in human blood plasma

The antibody capture method to evaluate the stoichiometry of inhibitor bound to TTR in human blood plasma has been described in detail elsewhere.[50] Briefly, 7.50 μL of a 1.44 mM DMSO solution of test compound was incubated with human blood plasma (1.00 mL) in a 2 mL Eppendorf tube in the dark at 37°C for 24 h on a rocker (30 rpm). Then, 125 μL of a 1:1 *v:v* slurry of unfunctionalized sepharose resin in TSA (10 mM Tris, pH 8.0, 140 mM NaCl) was added and the mixture was incubated for another hour at 4°C on a rocker (18 rpm). The sample was then centrifuged and the supernatant divided into 2 aliquots of 400 μL each, which were each added to 200 μL of a 1:1 *v:v* slurry of sepharose resin conjugated to an anti-TTR antibody in TSA, and the sample was incubated again at 4°C for 20 min on a rocker (18 rpm). The sample was then centrifuged, the supernatant removed, and the TTR-bound resin was washed three times (10 min each wash) with 1 mL TSA/0.05% saponin, then twice (10 min each wash) with 1 mL TSA at 4°C on a rocker (18 rpm). After centrifugation and removal of the final supernatant, dissociation of the TTR and bound test compound from the resin-bound antibody was achieved through addition of 155 μL of aqueous triethylamine (100 mM, pH~11.5) and rocking (18 rpm) at 4°C for 30 min. The suspension was then centrifuged and 135 μL of the supernatant, containing both TTR and test compound, was analyzed by RP-HPLC to determine the stoichiometry of small molecule bound to TTR (the test compound-TTR complex dissociates and the small molecule and protein are chromatographically separable under the HPLC buffer conditions). Quantification of test compound and TTR is achieved by comparing the integrated peak areas to standard curves: the ratio of the amount of test compound to TTR yields the binding stoichiometry, of which a theoretical maximum value of 2 is possible owing to the two T_4 binding sites per TTR tetramer. Analyses were performed in at least triplicates of duplicates from three different blood plasma samples (i.e. at least 6 analyses), with average values obtained presented in Figure 3 (errors are typically less than ±0.1).

Evaluating the inhibition of COX-1 enzymatic activity by the potent TTR amyloidogenesis inhibitors

The evaluation of the 18 most potent TTR aggregation inhibitors for inhibition of COX-1 activity was contracted out to the Cerep laboratories in Redmond, WA, USA. Compound analyses were performed using assay catalog reference #777−1hr, which uses procedures developed by Glaser *et al*.[44] A brief experimental protocol as provided by Cerep is outlined below. In this assay, the enzyme (~2 μg) is pre-incubated in the absence (water control) or presence of test compound (10.0 μM) for 20 min at 22°C in 250 μL of buffer (100 mM Tris-HCl, pH 8, 2 mM phenol, 1 μM hematine). Arachidonic acid (4 μM) is then added to initiate the reaction (no arachidonic acid added for basal control measurements). After incubation at 22°C for 10 min, the reaction is quenched by addition of 2 M HCl and 1 M Tris-HCl (pH 7.8) and cooling at 4°C. Prostaglandin-E_2 (PGE_2) quantification is performed using an EIA detection kit with measurements made using a microplate reader. Average values of duplicate analyses are presented in Figure 4 (black values), which represent the % inhibition of arachidonic acid conversion to PGE_2 due to competitive binding of test compound to COX-1 (errors of less than ±6 percentage points are representative of the data). Control analyses are performed analogously with the standard inhibitory reference compound, diclofenac, tested at several concentrations to obtain an inhibition curve from which its IC_{50} is calculated (12 nM).

Evaluating the binding of the potent TTR amyloidogenesis inhibitors to the thyroid hormone nuclear receptor

The evaluation of the 18 most potent TTR aggregation inhibitors for binding to the thyroid hormone receptor was contracted out to the Cerep laboratories in Redmond, WA, USA. Compound analyses were performed using assay catalog reference #855, which uses

procedures developed by Inoue *et al.*[45] A brief experimental protocol as provided by Cerep is outlined below. In this assay, liver membrane homogenates (100 μg protein) are incubated for 18 h at 4°C with 0.1 nM ^{125}I-labeled triiodothyronine ([^{125}I]T_3, the primary thyroid hormone) in the absence or presence of test compound (10.0 μM) in 500 μL of buffer (20 mM Tris-HCl, pH 7.6, 50 mM NaCl, 2 mM EDTA, 10% glycerol, and 5 mM β-mercaptoethanol). The samples are then vacuum filtered through glass fiber filters (GF/B, Packard), rinsed several times with ice-cold buffer (50 mM Tris-HCl and 150 mM NaCl), and the filters are dried and counted for radioactivity in a scintillation counter (Topcount, Packard) using a scintillation cocktail (Microscint 0, Packard). Non-specific binding, determined in the presence of 1 μM T_3, is subtracted from the [^{125}I]T_3 binding results. Average values of duplicate analyses are presented in Figure 4 (red italicized values), which represent the % displacement of [^{125}I]T_3 due to competitive binding of test compound to the thyroid hormone receptor (errors of less than ±2 percentage points are representative of the data). Control analyses are performed analogously with T_3 tested at several concentrations to obtain a competition curve from which its IC_{50} is calculated (0.38 nM).

X-Ray crystallographic analysis of WT-TTR bound to inhibitors 2c, 2d, 3d, 6d, and 10d

WT-TTR was purified from an *E. coli* expression system as described previously. The protein was concentrated to 4 mg/mL in 10 mM NaPi, 100 mM KCl, at pH 7.6 and co-crystallized at room temperature with various inhibitors at a 5 molar excess using the vapor-diffusion sitting drop method. Crystals were grown from 1.395 M sodium citrate, 3.5% *v/v* glycerol at pH 5.5. The crystals were cryo-protected with inhibitor-free 10% *v/v* glycerol. Data for **2c**, **2d**, **3d** were collected at beam line 5.0.2 at the Advanced Light Source (ALS) at wavelengths 1.000 Å. Data for **6d** were collected on the in-house source, a Rigaku FR-D (Cu-Ka) and MAR345dtb detector at 1.5417 Å. The data for **10d** were collected at beamline 9−2 at the SSRL at a wavelength of 0.9795 Å. All data sets were integrated and scaled using HKL2000.[51] The crystals were indexed in space group $P2_12_12$ with two subunits per asymmetric unit (see Table 1 for full data collection statistics). The five crystal structures were determined by molecular replacement with the initial model coordinates of 2FBR[38] using the program Phaser.[52] Further model building and refinement were completed using Refmac.53 For co-crystal structures **2c**, **2d**, **3d** and **10d**, hydrogens were added during refinement and anisotropic *B* values calculated. Final models were validated using the JCSG quality control server (http://jcsgsrv2/QC) incorporating Molprobity,[54] ADIT (http://rcsb-deposit.rutgers.edu/validate) WHATIF,[55] Resolve,[56] and Procheck.[57] Full data collection and refinement statistics are presented in Table 1.

Ligand energy calculations

Conformational energies of the compounds in their bound conformations were calculated using the MM2 and Dihedral Driver features of the Chem3D Ultra program (version 10.0), and compared to the calculated energies of the ligands in their energy-minimized unbound conformations.

Supplementary Material

Refer to Web version on PubMed Central for supplementary material.

Acknowledgements

We are grateful for the financial support of the NIH (DK 46335 to J.W.K and CA58896 and AI42266 to I.A.W, as well as the Skaggs Institute for Chemical Biology and the Lita Annenberg Hazen Foundation. Assistance with the thyroid hormone receptor and COX-I binding assays was provided by Richard Labaudiniere of FoldRx Pharmaceuticals (Boston, MA, USA). Technical support from Ted Foss, M. T. Dendle, and Mike Saure is also greatly appreciated. For structures **2c**, **2d**, and **3d,** X-ray diffraction data were collected at beamline 5.0.2 of the Advanced

Light Source (ALS) at Lawrence Berkeley Lab. The ALS is supported by the Director, Office of Science, and Office of Basic Energy Sciences of the U.S. Department of Energy under Contract No. DE-AC02-05CH11231. Data for structure **10d** were collected at beam line 9−2 at the Stanford Synchrotron Radiation Laboratory (SSRL), a national user facility operated by Stanford University on behalf of the U.S. Department of Energy, Office of Basic Energy Sciences. The SSRL Structural Molecular Biology Program is supported by the Department of Energy, Office of Biological and Environmental Research, and by the National Institutes of Health, National Center for Research Resources, Biomedical Technology Program, and the National Institute of General Medical Sciences. Data for structure **6d** was collected on the in-house source, a Rigaku FR-D (Cu-Ka) and MAR345dtb detector. The authors would also like to thank Drs. Xiaoping Dai, Andre Schiefner, and Xiaojin Xu in the Wilson laboratory for assistance with data collection.

Abbreviations

TTR, transthyretin; COX-1, cyclooxygenase-1; WT, wild type; HBP, halogen binding pocket; PGE_2, prostaglandin E_2; T_4, thyroxine; T_3, triiodothyronine; NSAID, non-steroidal anti-inflammatory drug.

References

1. Balch WE, Morimoto RI, Dillin A, Kelly JW. Adapting proteostasis for disease intervention. Science 2008;319:916–919. [PubMed: 18276881]
2. Zhang Q, Powers ET, Nieva J, Huff ME, Dendle MA, Bieschke J, Glabe CG, Eschenmoser A, Wentworth P Jr. Lerner RA, Kelly JW. Metabolite-initiated protein misfolding may trigger Alzheimer's disease. Proc. Natl. Acad. Sci. U.S.A 2004;101:4752–4757. [PubMed: 15034169]
3. Cohen E, Bieschke J, Perciavalle RM, Kelly JW, Dillin A. Opposing activities protect against age-onset proteotoxicity. Science 2006;313:1604–1610. [PubMed: 16902091]
4. Mu TW, Fowler DM, Kelly JW. Partial restoration of mutant enzyme homeostasis in three distinct lysosomal storage disease cell lines by altering calcium homeostasis. PLoS Biol 2008;6:e26. [PubMed: 18254660]
5. Dobson CM. Protein folding and misfolding. Nature 2003;426:884–890. [PubMed: 14685248]
6. Selkoe DJ. Folding proteins in fatal ways. Nature 2003;426:900–904. [PubMed: 14685251]
7. Johnson SM, Wiseman RL, Sekijima Y, Green NS, Adamski-Werner SL, Kelly JW. Native state kinetic stabilization as a strategy to ameliorate protein misfolding diseases: a focus on the transthyretin amyloidoses. Acc. Chem. Res 2005;38:911–921. [PubMed: 16359163]
8. Westermark P, Bergstrom J, Solomon A, Murphy C, Sletten K. Transthyretin-derived senile systemic amyloidosis: clinicopathologic and structural considerations. Amyloid 2003;10(Suppl 1):48–54. [PubMed: 14640042]
9. Westermark P, Sletten K, Johansson B, Cornwell GG 3rd. Fibril in senile systemic amyloidosis is derived from normal transthyretin. Proc. Natl. Acad. Sci. U.S.A 1990;87:2843–2845. [PubMed: 2320592]
10. Buxbaum JN, Tagoe CE. The genetics of the amyloidoses. Annu. Rev. Med 2000;51:543–569. [PubMed: 10774481]
11. Jiang X, Buxbaum JN, Kelly JW. The V122I cardiomyopathy variant of transthyretin increases the velocity of rate-limiting tetramer dissociation, resulting in accelerated amyloidosis. Proc. Natl. Acad. Sci. U.S.A 2001;98:14943–14948. [PubMed: 11752443]
12. Jacobson DR, Pastore RD, Yaghoubian R, Kane I, Gallo G, Buck FS, Buxbaum JN. Variant-sequence transthyretin (isoleucine 122) in late-onset cardiac amyloidosis in black Americans. N. Engl. J. Med 1997;336:466–473. [PubMed: 9017939]
13. Plante-Bordeneuve V, Said G. Transthyretin related familial amyloid polyneuropathy. Curr. Opin. Neurol 2000;13:569–573. [PubMed: 11073365]
14. Gambetti P, Russo C. Human brain amyloidoses. Nephrol. Dial. Transplant 1998;13(Suppl 7):33–40. [PubMed: 9870435]
15. Sekijima Y, Hammarstrom P, Matsumura M, Shimizu Y, Iwata M, Tokuda T, Ikeda S, Kelly JW. Energetic characteristics of the new transthyretin variant A25T may explain its atypical central nervous system pathology. Lab. Invest 2003;83:409–417. [PubMed: 12649341]

16. Hammarstrom P, Sekijima Y, White JT, Wiseman RL, Lim A, Costello CE, Altland K, Garzuly F, Budka H, Kelly JW. D18G transthyretin is monomeric, aggregation prone, and not detectable in plasma and cerebrospinal fluid: a prescription for central nervous system amyloidosis? Biochemistry 2003;42:6656–6663. [PubMed: 12779320]

17. Holmgren G, Ericzon BG, Groth CG, Steen L, Suhr O, Andersen O, Wallin BG, Seymour A, Richardson S, Hawkins PN. Clinical improvement and amyloid regression after liver transplantation in hereditary transthyretin amyloidosis. Lancet 1993;341:1113–1116. [PubMed: 8097803]

18. Tan SY, Pepys MB, Hawkins PN. Treatment of amyloidosis. Am. J. Kidney Dis 1995;26:267–285. [PubMed: 7645531]

19. Suhr OB, Herlenius G, Friman S, Ericzon BG. Liver transplantation for hereditary transthyretin amyloidosis. Liver Transpl 2000;6:263–276. [PubMed: 10827225]

20. Olofsson BO, Backman C, Karp K, Suhr OB. Progression of cardiomyopathy after liver transplantation in patients with familial amyloidotic polyneuropathy, Portuguese type. Transplantation 2002;73:745–751. [PubMed: 11907421]

21. Blake CC, Geisow MJ, Oatley SJ, Rerat B, Rerat C. Structure of prealbumin: secondary, tertiary and quaternary interactions determined by Fourier refinement at 1.8 Å. J. Mol. Biol 1978;121:339–356. [PubMed: 671542]

22. Hornberg A, Eneqvist T, Olofsson A, Lundgren E, Sauer-Eriksson AE. A comparative analysis of 23 structures of the amyloidogenic protein transthyretin. J. Mol. Biol 2000;302:649–669. [PubMed: 10986125]

23. Foss TR, Kelker MS, Wiseman RL, Wilson IA, Kelly JW. Kinetic stabilization of the native state by protein engineering: Implications for inhibition of transthyretin amyloidogenesis. J. Mol. Biol 2005;347:841–854. [PubMed: 15769474]

24. Foss TR, Wiseman RL, Kelly JW. The pathway by which the tetrameric protein transthyretin dissociates. Biochemistry 2005;44:15525–15533. [PubMed: 16300401]

25. Monaco HL, Rizzi M, Coda A. Structure of a complex of two plasma proteins: transthyretin and retinol-binding protein. Science 1995;268:1039–1041. [PubMed: 7754382]

26. Klabunde T, Petrassi HM, Oza VB, Raman P, Kelly JW, Sacchettini JC. Rational design of potent human transthyretin amyloid disease inhibitors. Nat. Struct. Biol 2000;7:312–321. [PubMed: 10742177]

27. Johnson SM, Connelly S, Wilson IA, Kelly JW. Biochemical and structural evaluation of highly selective 2-arylbenzoxazole-based transthyretin amyloidogenesis inhibitors. J. Med. Chem 2008;51:260–270. [PubMed: 18095641]

28. Johnson SM, Petrassi HM, Palaninathan SK, Mohamedmohaideen NN, Purkey H, Nichols C, Chiang KP, Walkup T, Sacchettini JC, Sharpless KB, Kelly JW. Bisaryloxime ethers as potent inhibitors of transthyretin amyloid fibril formation. J. Med. Chem 2005;48:1576–1587. [PubMed: 15743199]

29. Purkey HE, Palaninathan SK, Kent KC, Smith C, Safe SH, Sacchettini JC, Kelly JW. Hydroxylated polychlorinated biphenyls selectively bind transthyretin in blood and inhibit amyloidogenesis: rationalizing rodent PCB toxicity. Chem. Biol 2004;11:1719–1728. [PubMed: 15610856]

30. Oza VB, Petrassi HM, Purkey HE, Kelly JW. Synthesis and evaluation of anthranilic acid-based transthyretin amyloid fibril inhibitors. Bioorg. Med. Chem. Lett 1999;9:1–6. [PubMed: 9990446]

31. Oza VB, Smith C, Raman P, Koepf EK, Lashuel HA, Petrassi HM, Chiang KP, Powers ET, Sachettini J, Kelly JW. Synthesis, structure, and activity of diclofenac analogues as transthyretin amyloid fibril formation inhibitors. J. Med. Chem 2002;45:321–332. [PubMed: 11784137]

32. Petrassi HM, Johnson SM, Purkey H, Chiang KP, Walkup T, Jiang X, Powers ET, Kelly JW. Potent and selective structure-based dibenzofuran inhibitors of transthyretin amyloidogenesis: Kinetic stabilization of the native state. J. Am. Chem. Soc 2005;127:6662–6671. [PubMed: 15869287]

33. Petrassi HM, Klabunde T, Sacchettini JC, Kelly JW. Structure-based design of N-phenyl phenoxazine transthyretin amyloid fibril inhibitors. J. Am. Chem. Soc 2000;122:2178–2192.

34. Razavi H, Palaninathan SK, Powers ET, Wiseman RL, Purkey HE, Mohamedmohaideen NN, Deechongkit S, Chiang KP, Dendle MT, Sacchettini JC, Kelly JW. Benzoxazoles as transthyretin amyloid fibril inhibitors: synthesis, evaluation, and mechanism of action. Angew. Chem. Int. Ed. Engl 2003;42:2758–2761. [PubMed: 12820260]

35. Razavi H, Powers ET, Purkey HE, Adamski-Werner SL, Chiang KP, Dendle MT, Kelly JW. Design, synthesis, and evaluation of oxazole transthyretin amyloidogenesis inhibitors. Bioorg. Med. Chem. Lett 2005;15:1075–1078. [PubMed: 15686915]
36. Adamski-Werner SL, Palaninathan SK, Sacchettini JC, Kelly JW. Diflunisal analogues stabilize the native state of transthyretin. Potent inhibition of amyloidogenesis. J. Med. Chem 2004;47:355–374. [PubMed: 14711308]
37. Green NS, Foss TR, Kelly JW. Genistein, a natural product from soy, is a potent inhibitor of transthyretin amyloidosis. Proc. Natl. Acad. Sci. U.S.A 2005;102:14545–14550. [PubMed: 16195386]
38. Green NS, Palaninathan SK, Sacchettini JC, Kelly JW. Synthesis and characterization of potent bivalent amyloidosis inhibitors that bind prior to transthyretin tetramerization. J. Am. Chem. Soc 2003;125:13404–13414. [PubMed: 14583036]
39. Hammarstrom P, Wiseman RL, Powers ET, Kelly JW. Prevention of transthyretin amyloid disease by changing protein misfolding energetics. Science 2003;299:713–716. [PubMed: 12560553]
40. Wiseman RL, Johnson SM, Kelker MS, Foss T, Wilson IA, Kelly JW. Kinetic stabilization of an oligomeric protein by a single ligand binding event. J. Am. Chem. Soc 2005;127:5540–5551. [PubMed: 15826192]
41. Hammarstrom P, Schneider F, Kelly JW. Trans-suppression of misfolding in an amyloid disease. Science 2001;293:2459–2462. [PubMed: 11577236]
42. Coelho T, Carvalho M, Saraiva MJ, Alves I, Almeida MR, Costa PP. A strikingly benign evolution of FAP in an individual found to be a compound heterozygote for two TTR mutations: TTR Met 30 and TTR Met 119. J. Rheumatol 1993;20:179.
43. Coelho T, Chorao R, Sausa A, Alves I, Torres MF, Saraiva MJ. Compound heterozygotes of transthyretin Met30 and transthyretin Met119 are protected from the devastating effects of familial amyloid polyneuropathy. Neuromusc. Disord 1996;6:27. [PubMed: 8845715]
44. Glaser K, Sung ML, O'Neill K, Belfast M, Hartman D, Carlson R, Kreft A, Kubrak D, Hsiao CL, Weichman B. Etodolac selectively inhibits human prostaglandin G/H synthase 2 (PGHS-2) versus human PGHS-1. Eur. J. Pharmacol 1995;281:107–111. [PubMed: 8566109]
45. Inoue A, Yamakawa J, Yukioka M, Morisawa S. Filter-binding assay procedure for thyroid hormone receptors. Anal. Biochem 1983;134:176–183. [PubMed: 6318596]
46. Glenner GG. Amyloid deposits and amyloidosis: the beta-fibrilloses (second of two parts). N. Engl. J. Med 1980;302:1333–1343. [PubMed: 6990257]
47. Julius RL, Farha OK, Chiang J, Perry LJ, Hawthorne MF. Synthesis and evaluation of transthyretin amyloidosis inhibitors containing carborane pharmacophores. Proc. Natl. Acad. Sci. U.S.A 2007;104:4808–4813. [PubMed: 17360344]
48. Baures PW, Oza VB, Peterson SA, Kelly JW. Synthesis and evaluation of inhibitors of transthyretin amyloid formation based on the non-steroidal anti-inflammatory drug, flufenamic acid. Bioorg. Med. Chem 1999;7:1339–1347. [PubMed: 10465408]
49. Lashuel HA, Wurth C, Woo L, Kelly JW. The most pathogenic transthyretin variant, L55P, forms amyloid fibrils under acidic conditions and protofilaments under physiological conditions. Biochemistry 1999;38:13560–13573. [PubMed: 10521263]
50. Purkey HE, Dorrell MI, Kelly JW. Evaluating the binding selectivity of transthyretin amyloid fibril inhibitors in blood plasma. Proc. Natl. Acad. Sci. U.S.A 2001;98:5566–5571. [PubMed: 11344299]
51. Otwinowski Z, Minor W. Processing of X-ray diffraction data collected in oscillation mode. Methods Enzymol 1997;276:307–326.
52. Storoni LC, McCoy AJ, Read RJ. Likelihood-enhanced fast rotation functions. Acta Crystallogr. D Biol. Crystallogr 2004;60:432–438. [PubMed: 14993666]
53. Murshudov GN, Vagin AA, Dodson EJ. Refinement of macromolecular structures by the maximum-likelihood method. Acta Crystallogr. D Biol. Crystallogr 1997;53:240–255. [PubMed: 15299926]
54. Lovell SC, Davis IW, Arendall WB 3rd, de Bakker PI, Word JM, Prisant MG, Richardson JS, Richardson DC. Structure validation by Calpha geometry: phi,psi and Cbeta deviation. Proteins 2003;50:437–450. [PubMed: 12557186]
55. Vriend G. WHAT IF: a molecular modeling and drug design program. J. Mol. Graph 1990;8:52–56. 29. [PubMed: 2268628]

56. Terwilliger TC. Automated main-chain model building by template matching and iterative fragment extension. Acta Crystallogr. D Biol. Crystallogr 2003;59:38–44. [PubMed: 12499537]

57. Laskowski R, MacArthur M, Moss D, Thornton J. PROCHECK: A program to check the stereochemical quality of protein structures. J. Appl. Crystallogr 1993;26:283–291.

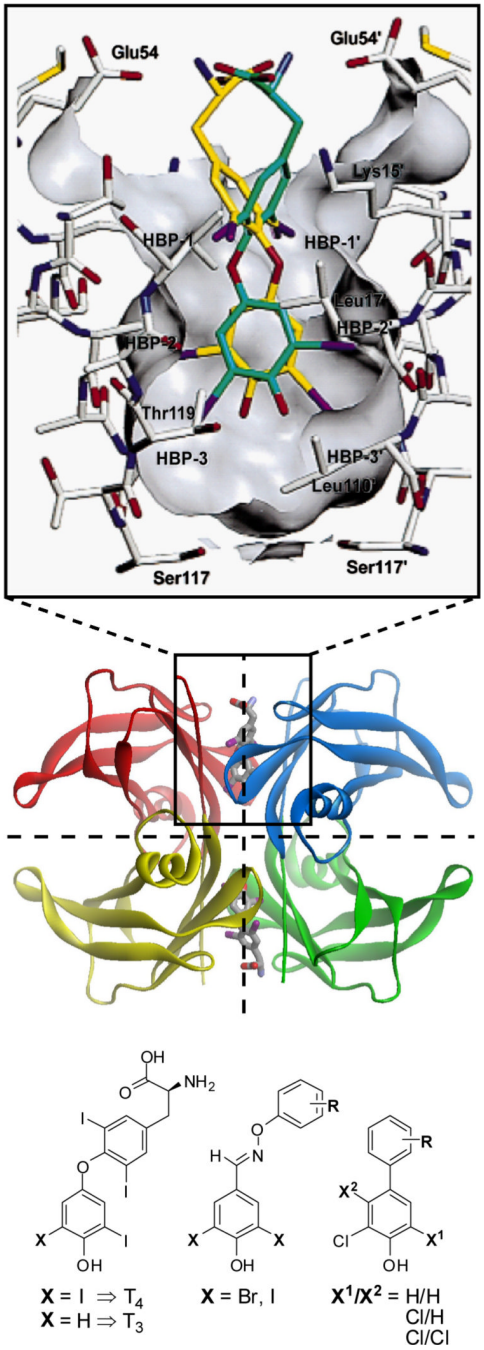

Figure 1.

Crystal structure (2ROX) of thyroxine (T_4) bound within the two pockets created by the weak dimer-dimer interface of tetrameric TTR (the two dimer-dimer interfaces are bisected by the dashed lines).[26] The expanded view of one site shows T_4 bound in its symmetry-related binding modes (green and yellow), with the binding site surface shown in grey (figure adapted from reference [26]). Primed amino acids or halogen binding pockets (HBPs) refer to symmetry-related monomers of TTR. Two structural series of inhibitors are shown below, the bisaryloxime ethers[28] and biphenyls[29] (**R** = variable substitution patterns of fluorine, chlorine, trifluoromethyl, carboxyl, or hydroxyl substituents), many of which are excellent TTR kinetic stabilizers that display high plasma TTR binding selectivity.

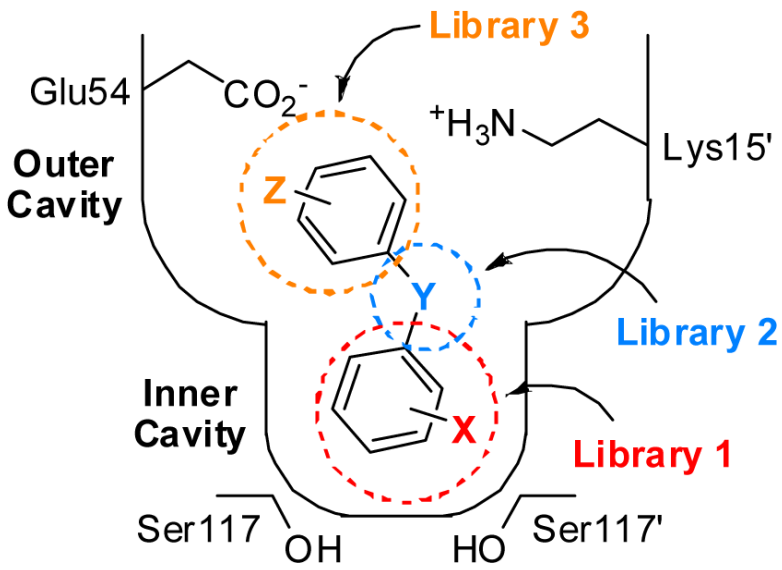

Figure 2.

Schematic depiction of one of the two T_4 binding pockets within TTR occupied by a typical small molecule TTR aggregation inhibitor. **Y** represents a linker of variable chemical structure (e.g. NH, O, CH-CH, C(O)NH, etc.) joining the two aryl rings, which typically bear a combination of alkyl, carboxyl, halide, trifluoromethyl, or hydroxyl substituents (**X** and **Z**). Library 2, being the focus of this manuscript, explores the SAR of the linker-**Y** substructure. While the aryl-**X** substructure was initially envisioned to bind within the inner cavity of the thyroxine binding site, previous crystallographic data reveal that molecules can bind opposite to the expected orientation.[26, 27, 29, 34, 36] Thus, it may not be the case that the aryl-**X** substructure of an inhibitor will occupy the inner binding cavity as illustrated. For conceptual simplicity in terms of integrating the data from the three inhibitor substructure optimization libraries, this initial schematic has been retained.

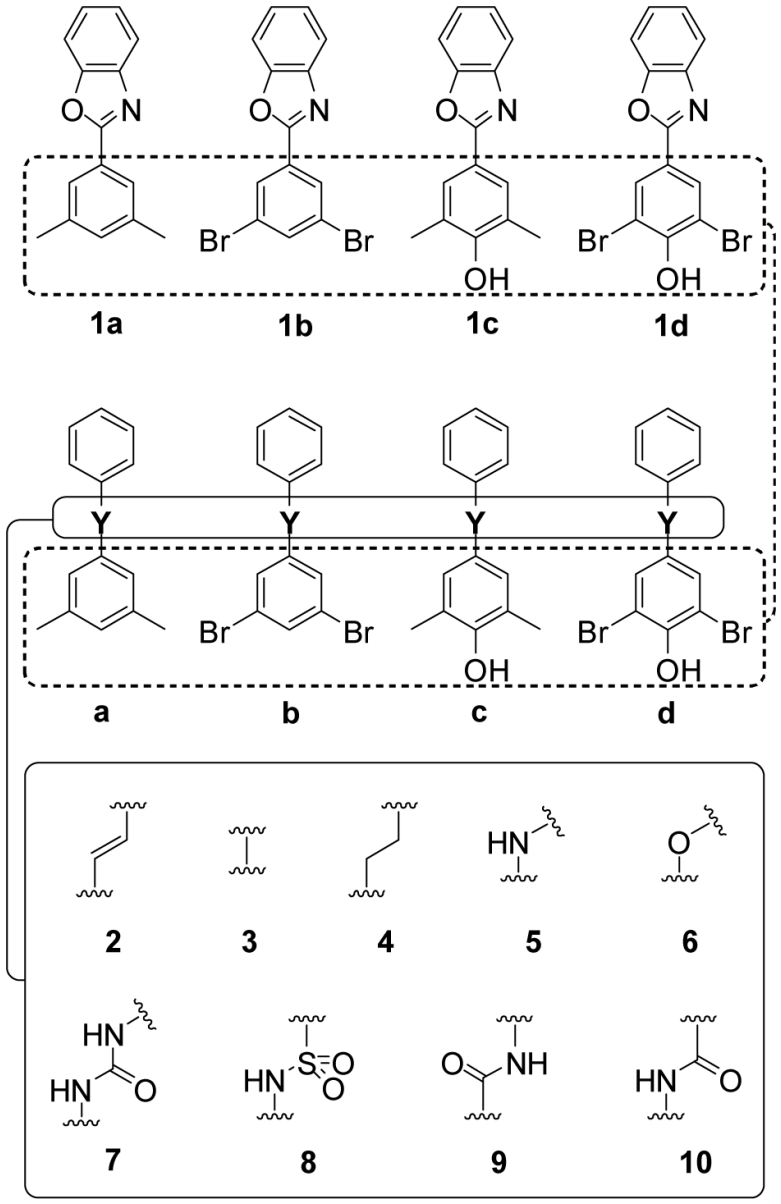

Figure 3.

Displayed are four potent TTR amyloidosis inhibitors (compounds **1a-d**) reported previously in our aryl-**X** optimization study.[27] The bisaryl scaffolds under evaluation in the current study are based on these four potent aryl-**X** substructures (**a-d**) to screen linker-**Y** substructures (**2**−**10**) for their ability to confer potent and selective inhibition of TTR amyloidogenesis, while minimizing COX-1 inhibition and thyroid hormone receptor binding.

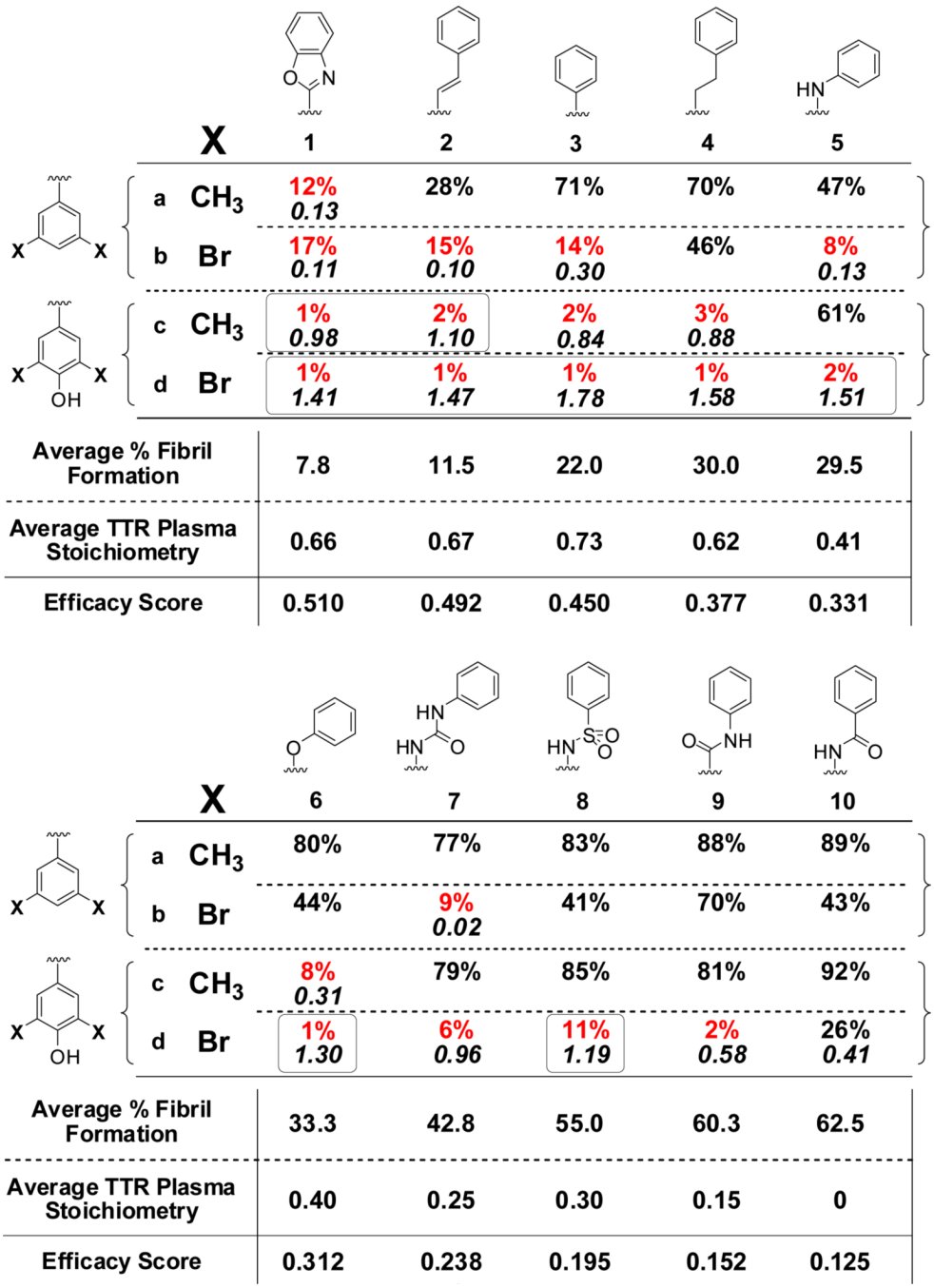

Figure 4.

Efficacy scoring of the different linker-**Y** substructures calculated from the TTR aggregation inhibition and plasma binding stoichiometry data. Percent (%) values represent the extent of WT-TTR fibril formation *in vitro* in the presence of inhibitor (7.2 μM inhibitor, 3.6 μM TTR, pH 4.4, 37°C, 72 h) relative to aggregation in the absence of inhibitor (100%), with the best values shown in red (< 20% aggregation; errors are typically less than ± 5 percentage points). The binding stoichiometries of the most potent aggregation inhibitors bound to TTR in human blood plasma *ex vivo* are shown in italics (10.8 μM inhibitor incubated with 1.8−5.4 μM TTR; theoretical maximum binding stoichiometry = 2). Those exhibiting exceptional binding selectivity to TTR are boxed (errors are typically less than ± 0.1). The efficacies of the different

linkers were quantitatively scored by entering the average % fibril formation (% $F.F._{ave}$) and average TTR plasma binding stoichiometry ($P.S._{ave}$) values into equation **1** (values averaged over the four inhibitors in each linker series – compounds displaying > 20% fibril formation were assigned TTR plasma binding stoichiometries of 0 for these calculations). Higher efficacy scores correspond to more potent and selective substructures.

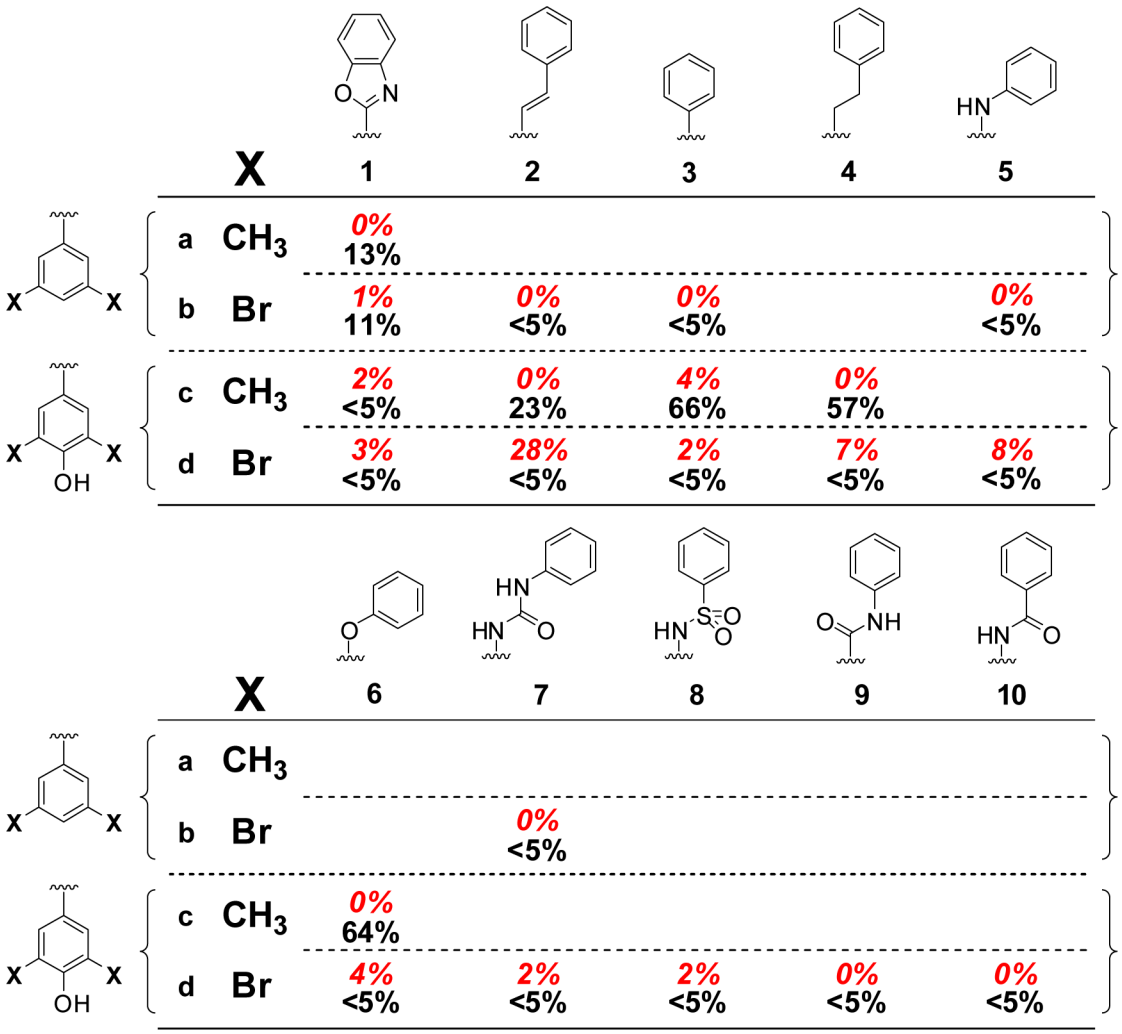

Figure 5.

Thyroid hormone receptor T_3 displacement and COX-1 inhibition for the most potent aggregation inhibitors. The extent of inhibitor that displaces T_3 from the thyroid hormone receptor is shown in red italics (errors are typically less than ±2 percentage points). COX-1 inhibition results are shown below in black, with values representing the % inhibition by the test compounds of COX-1 mediated conversion of arachidonic acid to prostaglandin-E_2 (errors are typically less than ±6 percentage points).

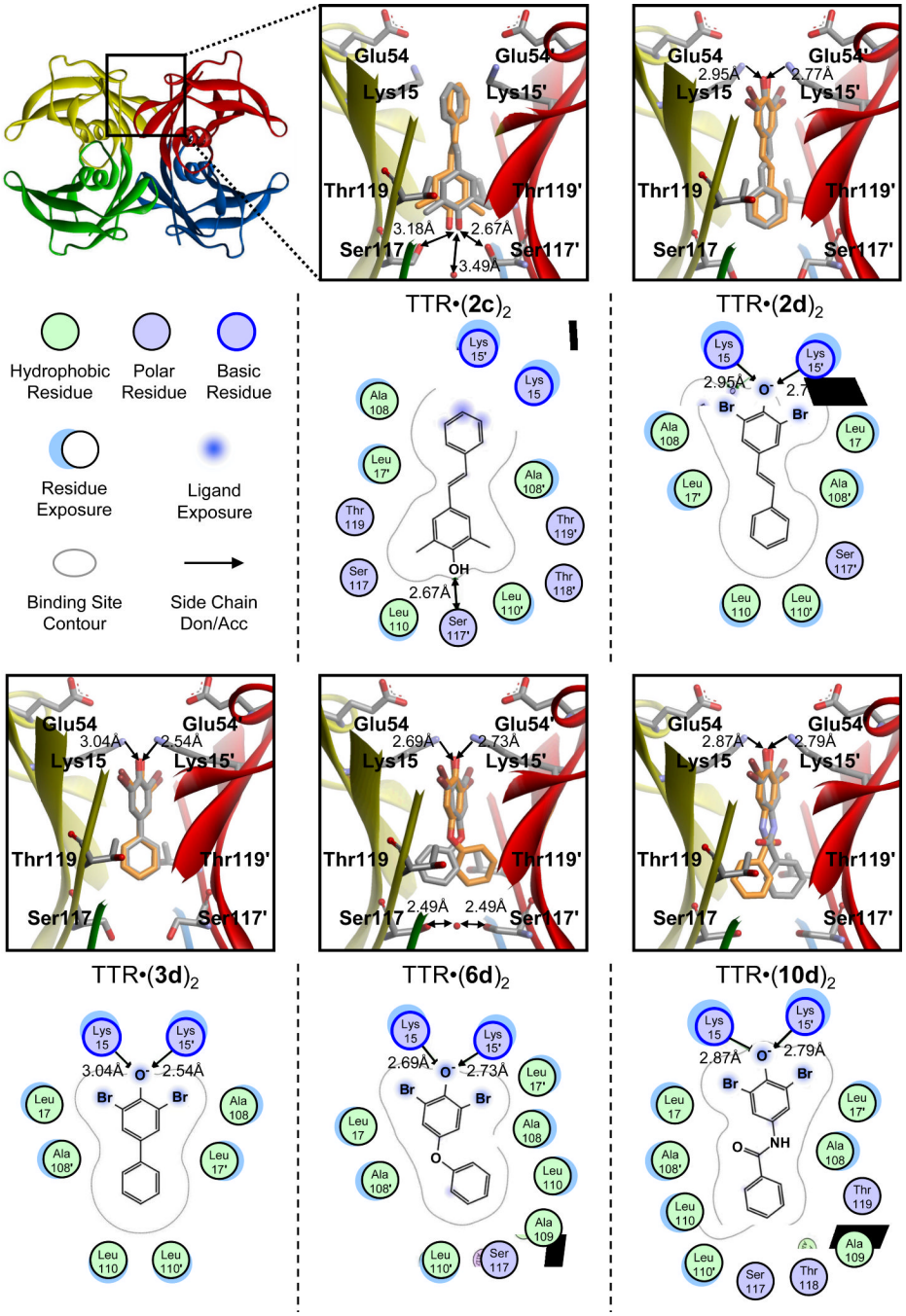

Figure 6.

X-ray crystallography structures and schematics of key features of homotetrameric WT-TTR co-crystallized with inhibitors **2c, 2d, 3d, 6d, and 10d** (PDB ascession codes 3CN0, 3CN1, 3CN2, 3CN3, 3CN4, respectively). Individual TTR monomers in the three-dimensional ribbon diagrams have been color coded red, yellow, green, and blue for differentiation. Zoomed images show inhibitors bound in their two symmetry-related binding modes (orange and grey) in one of the two symmetrical thyroxine binding sites, appearing superimposed on one another owing to their positioning on the crystallographic C_2 axis. The ordered water molecules bridging the Ser117 and 117' hydroxyls of adjacent TTR monomers in the TTR•(**2c**)$_2$ and TTR•(**6d**)$_2$ structures are shown as red spheres. Important hydrogen bonding and electrostatic

interactions between protein side chains and the ligands (or H_2O, as in the case of TTR•(**2c**)$_2$ and TTR•(**6d**)$_2$ structures) are indicated by arrows, with distances shown in Å. Schematic representations of each bound inhibitor are presented as two-dimensional topology diagrams (generated using MOE (2006.08), Chemical Computing Group, Montreal, Canada). In these schematic diagrams, inhibitors are shown in only one of their symmetry-related binding modes for clarity. A graphical legend for interpretation of key binding site characteristics is displayed below the TTR tetramer ribbon diagram at the top left. Ligand exposure indicates specific portions of the ligand structures that are solvent accessible (i.e. not completely buried within the binding pocket). Residue exposure indicates those amino acids for which their side chains and/or peptide backbones are partially solvent accessible.

Table 1

Data collection and refinement statistics for the crystal structures of WT-TTR in complex with inhibitors **2c**, **2d**, **3d**, **6d**, and **10d**.

	WT-TTR/2c	WT-TTR/2d	WT-TTR/3d	WT-TTR/6d	WT-TTR/10d
Data Collection					
Beamline	ALS 5.0.3	ALS 5.0.3	ALS 5.0.3	In-House	SSRL 9−2
Wavelength (Å)	1.0000	1.0000	1.0000	1.5417	0.9795
Resolution (Å)	1.52 (1.51−1.56)[a]	1.52 (1.51−1.56)	1.52 (1.51−1.56)	1.80 (1.80−1.86)	1.40 (1.40−1.45)
Space group	$P2_12_12$	$P2_12_12$	$P2_12_12$	$P2_12_12$	$P2_12_12$
a, *b*, *c* (Å)	43.02,85.56,64.52	42.74,85.04,60.09	43.05,85.21, 64.81	42.86,84.87,64.79	42.61, 85.23,64.32
No. of molecules in the a.u.	2	2	2	2	2
No. of observations	257,563 (22,509)[a]	238,854 (15,789)	261,723 (25,064)	154,054 (14,867)	318,115 (22,599)
No. of unique reflections	37,877 (3,690)[a]	36,190 (3,096)	37,389 (3,686)	22,655 (2219)	45,445 (4,109)
Redundancy	6.8 (6.1)[a]	6.6 (5.1)	7.0 (6.8)	6.8 (6.7)	7.0 (5.5)
Completeness (%)	99.6 (99.0)[a]	96.9 (84.5)	99.4 (100.0)	99.9 (100.0)	96.9 (89.8)
R_{sym} (%)[b]	4.4 (22.7)[a]	5.8 (25.7)	5.8 (20.3)	4.0 (14.7)	3.3 (42.6)
Average I/σ	34.6 (7.3)[a]	27.2 (4.9)	23.2 (11.6)	44.2 (13.8)	39.8 (3.5)
Refinement statistics					
Resolution (Å)	1.52−50.00	1.52−50.00	1.52−50.00	1.80−50.00	1.40−50.00
No. of reflections (working set)	35,449 (2,568)[a]	34,319 (2,141)	35,400 (2,594)	21,396 (1,525)	43,118 (2,804)
No. of reflections (test set)	1,858 (145)[a]	1,815 (114)	1,859 (132)	1,157 (104)	2,292 (153)
R_{cryst} (%)[a,c]	16.0 (14.1)[a,c]	16.1 (13.3)	16.4 (14.3)	17.0 (21.6)	17.3 (29.8)
R_{free} (%)[a,d]	18.8 (23.6)[a,d]	18.8 (19.9)	19.7 (18.8)	21.6 (30.1)	20.1 (32.6)
No. Protein/Ligand/Water atoms	891,884/34/126	891,884/34/132	891,884/30/135	891,884/32/103	891,884/36/126
Average B-values (Å)					
Protein	15.2	15.5	15.3	21.2	17.0
Ligand	30.3	22.5	23.9	22.8	29.7
Wilson *B*-value	18.0	17.5	18.1	22.1	20.7
Ramachandran plot					
Most favored (%)	92.1	92.1	93.1	89.1	92.1
Additionally allowed (%)	7.9	7.9	6.9	10.9	7.9
Generously allowed (%)	0	0	0	0	0
Disallowed (%)	0	0	0	0	0
R.M.S. deviations					
Bond lengths (Å)	0.019	0.019	0.019	0.019	0.018
Angles (°)	1.73	1.77	1.72	1.62	1.79

[a] Numbers in parentheses are for highest resolution sell of data.

[b] $R_{sym} = \Sigma_{hkl} | I-\langle I\rangle | \Sigma_{hkl} I$

[c] $R_{cryst} = \Sigma_{hkl} | F_O-F_C | \Sigma_{hkl} F_O$

[d] R_{free} is the same as R cryst, but for 5% of data excluded from the refinement.